

# Computation of fluid flow and pore-space properties estimation on micro-CT images of rock samples

M. Starnoni<sup>a,\*</sup>, D. Pokrajac<sup>a</sup>, J. E. Neilson<sup>b</sup>

<sup>a</sup>*School of Engineering, University of Aberdeen, King's College, Aberdeen AB24 3UE Scotland, United Kingdom*

<sup>b</sup>*Department of Geology and Petroleum Geology, University of Aberdeen, King's College, Aberdeen AB24 3UE Scotland, United Kingdom*

---

## Abstract

Accurate determination of the petrophysical properties of rocks, namely REV, mean pore and grain size and absolute permeability, is essential for a broad range of engineering applications. Here, the petrophysical properties of rocks are calculated using an integrated approach comprising image processing, statistical correlation and numerical simulations. The Stokes equations of creeping flow for incompressible fluids are solved using the Finite-Volume SIMPLE algorithm. Simulations are then carried out on three-dimensional digital images obtained from micro-CT scanning of two rock formations: one sandstone and one carbonate. Permeability is predicted from the computed flow field using Darcy's law. It is shown that REV, REA and mean pore and grain size are effectively estimated using the two-point spatial correlation function. Homogeneity and anisotropy are also evaluated using the same statistical tools. A comparison of different absolute permeability estimates is also presented, revealing a good agreement between the numerical value and the experimentally determined one for the carbonate sample, but a large discrepancy for the sandstone. Finally, a new convergence criterion for the SIMPLE algorithm, and more generally for the family of pressure-correction methods, is presented. This criterion is based on satisfaction of bulk momentum balance, which makes it particularly useful for pore-scale modelling of reservoir rocks.

*Keywords:* Digital rock physics, Permeability estimation, Carbonate, Finite-Volume SIMPLE, Two-point correlation, Micro-Computer Tomography

---

## 1. Introduction

Fluid flow in porous media is encountered in many practical engineering problems, including oil, water and gas flow in petroleum reservoirs, transport of water and contaminants in unsaturated soils, heating and drying in industrial processes and storage of  $CO_2$  in deep underground aquifers.

The importance of pore-scale simulations lays on the fact that fluid properties, geometry of the medium and boundary conditions are much easier to systematically investigate in computer simulations rather than experiments, and that we can use the results obtained from pore-scale simulations to reduce uncertainties in predicting larger-scale phenomena. Advances in pore-space visualization to very high image resolution and constant increase in computer power also contributed to the popularity of this field of study. In particular, image acquisition techniques have advanced from statistical reconstruction of three-dimensional representations of the pore-space based on two-dimensional images, to three-dimensional images directly produced by micro-Computer Tomography ( $\mu$ -CT). With modern  $\mu$ -CT scanners, an

---

\*Corresponding author

Email address: [michele.starnoni@gmail.com](mailto:michele.starnoni@gmail.com) (M. Starnoni)  
Preprint submitted to Elsevier

instrument housing its own source of X-rays, the 3D representation of the pore-space is reconstructed from a series of 2D projections taken at different angles, allowing for reproducing the exact microstructure of a rock sample down to a resolution of 1  $\mu\text{m}$ . This enables predictions to be made on many 3D images of small rock samples, providing data that would be much more difficult or impossible to obtain using traditional experiments. A recent review on pore-scale imaging and modelling can be found in Blunt et al. (2013).

There are two ways to compute pore-space properties: network modelling and direct simulations. In network modelling (Bakke et al., 1997; Oren et al., 1998; Blunt et al., 2002; Valvatne et al., 2005), the complex geometry of the medium is replaced by a topologically representative system of larger void spaces called pores, connected by straight channels called throats. In direct simulations instead, the real pore-space of the medium is the solution domain for the governing equations. Lattice Boltzmann methods (LBM) (Frisch et al., 1986; Chen and Doolen, 1998; Zu and He, 2013) are the most popular approach for computing single and multiphase flow directly on pore-space images. LBM has a kinetic nature and consists of a number of particles moving in a regular lattice and undergoing momentum-conserving collisions. The resulting fluid properties are then obtained by statistical averaging. LBM can also be seen as a discretization of the Boltzmann equation for a particle velocity distribution field.

Another more traditional direct approach involves solving the Navier-Stokes equations using conventional grid based methods such as finite difference (FD), finite element (FE) and finite volume (FV). Pioneering investigations in this field are due to Adler et al. (1990). They computed permeability values on a fictitious porous medium, sharing the same statistical properties of real Fontainebleau sandstones, and then compared the numerical values with experimental data. They found the predicted permeabilities five times greater than the measured ones, although the general shape of the experimental curve was well-reproduced. Martys et al. (1994) and Coelho et al. (1997) simulated fluid flow and dispersion through random packings of spheres and packings of grains of arbitrary shape respectively, in order to obtain universal curves for fluid permeability. Their data were found to agree well with experimentally obtained permeability values of several sandstones. The first use of 2D digital images of real porous microstructures, captured using an optical microscope, is due to Tashman et al. (2003). They first validated the numerical scheme by comparing the predicted permeability values of a medium of packed columns to a closed form solution, and then evaluated the permeability tensor of three natural granular microstructures (Glass beads of 1 mm diameter and two sands with an average particle diameter between 0.40 and 0.60 mm). Al-Omari and Masad (2004) computed fluid flow in 3D microstructures of field cores of asphalt mixes, captured using X-rays CT, with average particle diameter between 3 and 10 mm, and compared the predicted permeability values with closed form solutions. Zaretskiy et al. (2010) applied the FE method to study a digitized Fontainebleau sandstone sample, comparing their numerical performance to LBM simulations. Mostaghimi et al. (2013) simulated Stokes flow directly on pore-space images obtained from  $\mu$ -CT scanning of a range of porous microstructures, including sandstones (mean pore radius 15-20  $\mu\text{m}$ ) and carbonates (mean pore radius 10-15  $\mu\text{m}$ ) (Dong, 2008). They studied the existence and size of the representative elementary volume (REV) (Bear, 1972) showing that the REV for permeability is

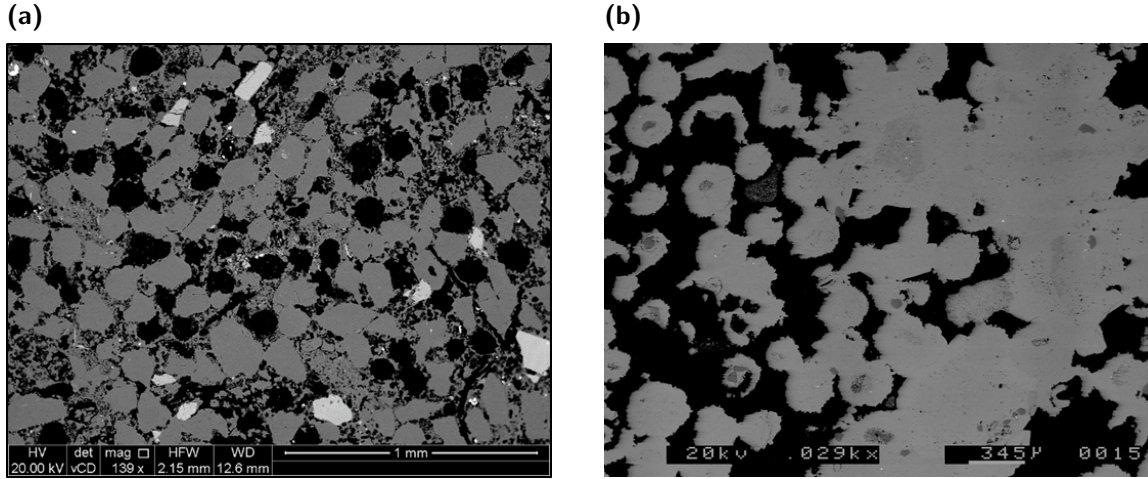


Figure 1. 2D SEM images of the CB sandstone (a) and carbonate (b) rocks

60 larger than for other static properties, such as porosity. Guibert et al. (2015) investigated the role of  
 61 mesh sensitivity in computing permeability on a Dausse sandstone, showing that mesh refinement of the  
 62 original tomographic image has a non-negligible impact on the evaluation of the permeability tensor.

63 The same approach of using combined high-resolution imaging and numerical simulations has also  
 64 been used by other researchers in the area of stochastic reconstruction (Øren and Bakke, 2002; Politis  
 65 et al., 2008) and other fields such as fuel cells (Litster et al., 2013; Sabharwal et al., 2016). In stochastic  
 66 reconstruction studies, numerical simulations are accompanied by statistical analyses. Statistical analyses  
 67 offer a valuable tool for characterizing the porous microstructure, and hence are used for assisting in the  
 68 reconstruction process. However, these studies overall focus on the reconstruction process itself rather  
 69 than on the characterization of real media. Likewise, fuel cells studies work on the nano-scale, and hence  
 70 investigate physical processes rather different from those occurring at the micro-scale investigated in  
 71 digital rock physics. Moreover, they do not simulate Stokes flow, nor explore permeability.

72 In this paper, we extended the analyses presented in previous studies and developed an integrated  
 73 approach, comprising rock imaging, statistical spatial correlation and numerical simulations, for thorough  
 74 characterization of reservoir rocks. Our study is carried out on 3D digital images obtained from  $\mu$ -CT  
 75 scanning of two rock formations: one sandstone and one carbonate. The morphological properties of the  
 76 rocks and the image processing techniques adopted are described in Sec. 2. Then, statistical correlation  
 77 tools are illustrated in Sec. 3. Next, in Sec. 4, results of single-phase flow simulations are presented, and a  
 78 comparison of various permeability estimates obtained from different approaches is made. Finally, a novel  
 79 convergence criterion for the SIMPLE algorithm, and more generally for the family of pressure-correction  
 80 methods, based on bulk momentum balance, is presented in Sec. 5.

## 81 2. Rocks description and Image processing

82 Core plugs of two rock formations are used in this work: one sandstone (Fig. 1a) and one carbon-  
 83 ate (Fig. 1b). Cylindrical cores of the former one (5 cm long and 3.75 cm in diameter) were drilled  
 84 from a single sample block of Jurassic Lower Calcareous Gritstone Formation from Cayton Bay (CB),  
 85 Scarborough (UK). The cores consist mainly of quartz (76%), muscovite (7.5%) and mitrocline (6.5%)

86 with a range of Calcite comprising about 4-5% of the rock mass. Measured porosity and permeability  
87 were ranging between 30.5% and 35% (average 33%) and from 8 to 12 mDa respectively. Porosity was  
88 measured by Helium expansion and NMR, while permeability was calculated by injecting low-salinity  
89 brine (1 NaCl) through rock cores at room temperature and Confinement pressure of 10 MPA, and using  
90 Darcy's law (Lamy-Chappuis, 2015). Mean pore diameter observed from Scanning Electron Microscope  
91 (SEM) images is 100  $\mu\text{m}$ . Further details on the morphology of this rock can be found in Lamy-Chappuis  
92 et al. (2014).

93 The second rock formation studied is a carbonate of late Cambrian age. This was cut from an  
94 outcrop sample of the Al Bashair Formation, Huqf High, Oman. It is an oolitic grainstone (grains  
95 range in size from 200-480  $\mu\text{m}$ , median 330  $\mu\text{m}$ ) with scattered lime mudstone clasts up to 3 cm in  
96 length ( $< 1$  cm thickness). The sample is composed entirely of calcite and, despite its age, contains  
97 significant intergranular porosity which has been solution enhanced forming small vugs in places. The  
98 intergranular/vuggy pore spaces observed in SEM images range from 90  $\mu\text{m}$  to 700  $\mu\text{m}$  diameter, together  
99 with microporosity ( $< 20$   $\mu\text{m}$ ) within grains (Haines et al., 2015). As with many carbonate samples, the  
100 pore system is heterogeneous. Porosity of 15.98% and permeability of approximately 1500 mDa were  
101 measured on a 4.48 cm in length and 2.53 in diameter core plug. A Coberly-Stevens porosimeter was  
102 used to measure the He-porosity on the core plug at ambient temperature and pressure conditions. He-  
103 porosity was calculated using the method outlined in Haines et al. (2015, 2016). A Jones Nitrogen  
104 permeameter was used to calculate steady-state permeability on the same core plug according to Darcy's  
105 Law, by measuring the flow rate of nitrogen through the core plugs at ambient temperature and pressure,  
106 using the method described in Haines et al. (2016). A specimen was then manually detached from the  
107 core plug and scanned.

108 CT imaging of the sandstone sample was carried out using a  $\mu$ -CT scanner housed in the Department  
109 of Mechanical Engineering, University of Leeds, at 5 and 10  $\mu\text{m}$  pixel resolution (Lamy-Chappuis, 2015).  
110 The carbonate sample was scanned using Zeiss XRadia Versa 410 microscope with a 140kV/10W X-rays  
111 source housed in the School of Engineering, University of Aberdeen, at pixel resolution of 8.3  $\mu\text{m}$  and  
112 the field of view covering 16.6 x 16.6 x 16.6 mm (see Fig. 2). Acquisition of 2D and the reconstruction  
113 of 3D images was performed using the software supplied by the respective manufacturers. The latter  
114 step involved applying an optimum pixel shift in order to compensate for a slight miss-alignment of the  
115 centre of rotation for the sample bottom and top, and an optimum beam hardening constant in order  
116 to minimise the effect of beam hardening. Both stages of the process were first done automatically and  
117 then checked visually to make sure that the reconstructed pore space does not contain any artefacts.  
118 Manual thresholding of the reconstructed 3D images, with threshold level firstly determined using Otsu's  
119 method (Otsu, 1975) and then adjusted in such a way to match the experimentally measured porosity,  
120 produced 3D binary models consisting of void and solid voxels. A final visual inspection was conducted  
121 to verify that the pore space was segmented correctly. Different sub-samples were then extracted from  
122 these initial binary images and used as FV meshes. For the sandstone, sub-samples from three different  
123 locations were taken (CBSandstone1, 2 and 3) while for the carbonate, sub-samples were extracted by

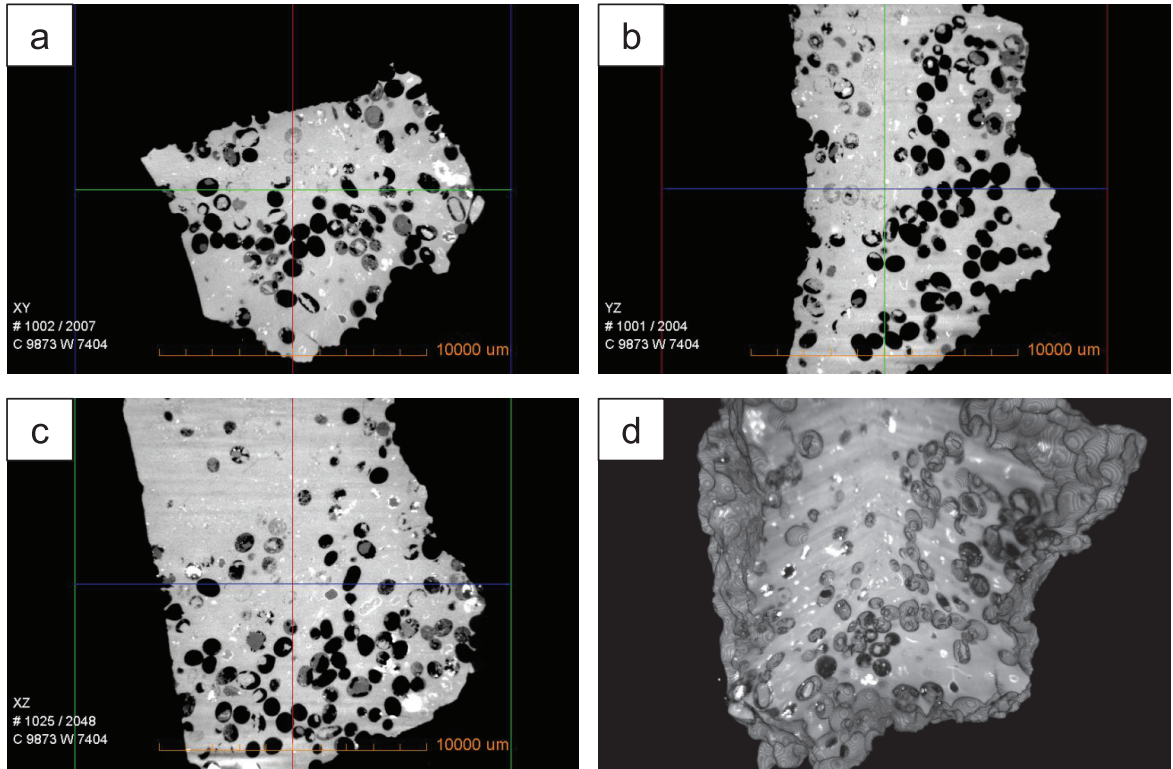


**Figure 2.** CT imaging of the carbonate sample: 2D sections corresponding to the three orthogonal planes (a, b and c) and the reconstructed 3D microstructure (d)

**Table 1.** List of samples used in this study

Sample	Size [mm <sup>3</sup> ]	Resolution [ $\mu$ m]	Voxels	$\phi$ [%]
CBsandstone1a	1	10	100 <sup>3</sup>	31.9
CBsandstone1b	1	5	200 <sup>3</sup>	32.1
CBsandstone2	1	5	200 <sup>3</sup>	30.9
CBsandstone3	8	5	400 <sup>3</sup>	29.6
Carb200	4.6	8.3	200 <sup>3</sup>	16.5
Carb300	15.6	8.3	300 <sup>3</sup>	15.8
Carb400	36.6	8.3	400 <sup>3</sup>	15.9
Carb500	71.5	8.3	500 <sup>3</sup>	15.8

124 keeping a fixed origin point and considering cubic volumes of increasing size centered at this point.

125 A list of all the sub-samples considered in this study is given in Table 1 while Fig. 3 shows an example  
 126 of the reconstructed microstructures for both the rocks.

### 127 3. Two-point spatial correlation function

128 A binary indicator function  $\xi$  is defined for any position  $\mathbf{x}$  in the medium as follows

$$\xi(\mathbf{x}) = \begin{cases} 1, & \text{if } \mathbf{x} \text{ is in the pore space,} \\ 0, & \text{if } \mathbf{x} \text{ is in a grain.} \end{cases} \quad (1)$$

129 The two-point correlation function  $Z_2$  is defined as the probability that two points separated by a distance  
 130  $\mathbf{r}$  will both lie in the pore space and is mathematically given by (Berryman, 1985; Berryman and Blair,  
 131 1986)

$$Z_2(\mathbf{r}) = \langle \xi(\mathbf{x})\xi(\mathbf{x} + \mathbf{r}) \rangle, \quad (2)$$

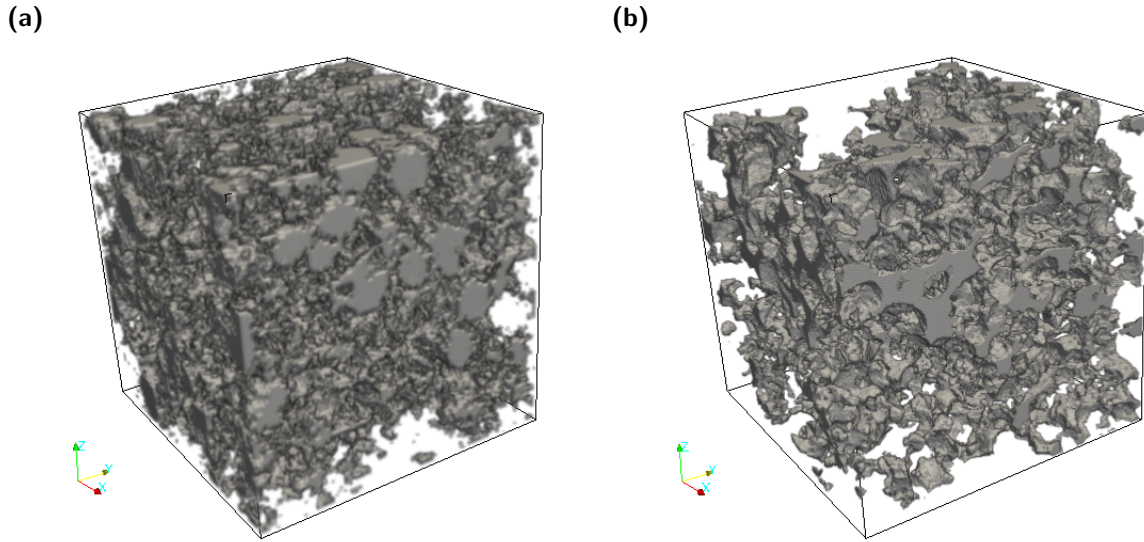


**Figure 3.** Reconstructed 3D digital images of the samples CBsandstone1a (a) and Carb300 (b)

132 where angle brackets denote superficial volume averaging over all positions  $\mathbf{x}$  and  $Z_2(0) = \phi$ . The two-  
 133 point correlation for a 2D digital image is computed using the one-dimensional isotropic method by  
 134 Berryman (1985). The discrete form of eq. (2) for progressive one-pixel increments  $k$  is given by

$$Z_2(k) = \frac{1}{2k+1} \sum_{l=0}^{2k} \bar{Z}_2(k \cos \varphi, k \sin \varphi), \quad \varphi = \frac{\pi l}{4k}, \quad 0 \leq k \leq N/2, \quad (3)$$

135 where  $N$  is the number of pixels along each side of the image and the discrete function  $\bar{Z}_2(m, n)$  has the  
 136 form

$$\bar{Z}_2(m, n) = \frac{1}{N_{max}} \sum_{\substack{1 \leq i \leq i_{max} \\ 1 \leq j \leq j_{max}}} \xi_{ij} \xi_{i+m, j+n}, \quad (4)$$

137 where  $i_{max} = N - m$ ,  $j_{max} = N - n$  and  $N_{max} = i_{max} j_{max}$ . The procedure is schematically illustrated in  
 138 Fig. 4. The discrete two-point correlation function  $\bar{Z}_2$  is computed at points located along the perimeters  
 139 of arcs centered at the reference point. The arcs are delimited by values of  $\varphi$  equal to 0 and  $\frac{\pi}{2}$  and their  
 140 radii are equal to the increment  $k$ . For each increment  $k$ ,  $\bar{Z}_2$  is evaluated separately along  $(2k+1)$   
 141 directions  $\varphi$ , and then averaged to compute the one-dimensional isotropic function  $Z_2$ . Each node of the  
 142 image is in turn used as reference point, and all segments whose endpoint lies within the image are used  
 143 for computing  $\bar{Z}_2$ . When  $\varphi$  takes values other than 0 and  $\frac{\pi}{2}$ , i.e. the discrete point does not coincide with  
 144 a lattice node,  $\bar{Z}_2(m, n)$  is computed using bilinear interpolation from the 4 closest nodes. The extension  
 145 to the 3D case is straightforward, with eqs. (3) and (4) which modify as follows

$$Z_2(k) = \frac{1}{(2k+1)^2} \sum_{l_1, l_2=0}^{2k} \bar{Z}_2(k \sin \theta \cos \varphi, k \sin \theta \sin \varphi, k \cos \theta), \quad (5)$$

$$\theta = \frac{\pi l_1}{4k}, \quad \varphi = \frac{\pi l_2}{4k}, \quad 0 \leq k \leq N/2,$$

146

$$\bar{Z}_2(m, n, o) = \frac{1}{N_{max}} \sum_{\substack{1 \leq i \leq i_{max} \\ 1 \leq j \leq j_{max} \\ 1 \leq k \leq k_{max}}} \xi_{ijk} \xi_{i+m, j+n, j+o}, \quad (6)$$

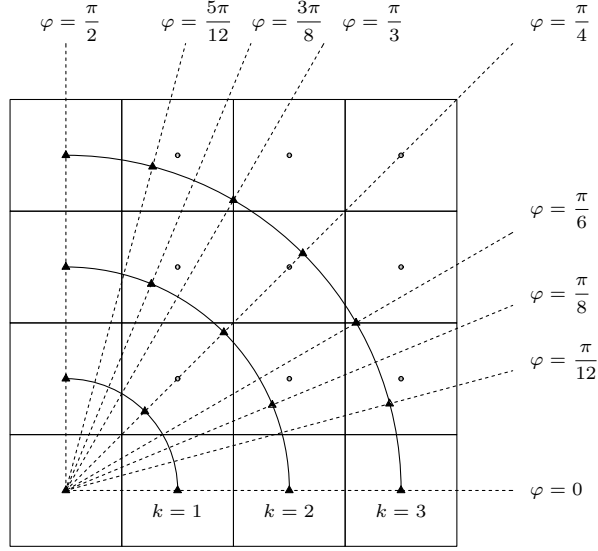


**Figure 4.** Schematic of the method employed for computing the one-dimensional isotropic two-point correlation function  $Z_2(k)$  on a 2D digital image (Berryman, 1985). The discrete two-point correlation function  $\bar{Z}_2$  is computed at triangular points located along the perimeters of circles centered at the reference point. The circles radii are 1 pixel ( $k=1$ ), 2 pixels ( $k=2$ ), etc.

147 where  $k_{max} = N - o$ ,  $N_{max} = i_{max}j_{max}k_{max}$  and  $\bar{Z}_2(m, n, o)$  is computed using trilinear interpolation  
 148 from the 8 closest nodes when the discrete point does not coincide with a lattice node.

149 This correlation function has the relevant feature that many physical properties of the porous material,  
 150 such as porosity  $\phi$ , pore-grain specific surface area  $s$  and effective pore size  $r_c$ , can be obtained from it.  
 151 Berryman and Blair (1986) showed that

$$\lim_{r \rightarrow \infty} Z_2(\mathbf{r}) = \phi^2, \quad (7)$$

$$Z_2'(0) = -\frac{s}{\chi}, \quad (8)$$

$$r_c = \frac{\phi(1 - \phi)}{Z_2'(0)}, \quad (9)$$

152 where  $\chi$  is 4 for 2D and 6 for 3D images (Yeong and Torquato, 1998) and the initial slope  $Z_2'(0)$  is  
 153 computed using ordinary least squares to the first four or five points of the curve. Specific surface area  
 154 can then be used to estimate the absolute permeability  $K$  following the Kozeny-Carman (KC) approach.  
 155 KC empirical formulations relate permeability to porosity and hydraulic radius, the latter defined as the  
 156 ratio of the pore volume and the wetted area. The KC relation developed by Walsh and Brace (1984) is  
 157 used here:

$$K = \frac{\phi^2}{m_1 F s^2}, \quad (10)$$

158 where  $m_1$  is a constant depending on the pore shape (2 for circular tubes and 3 for cracks) and  $F$  is the  
 159 electrical formation factor which can be estimated using the relationship given by Archie et al. (1942)

$$F = \phi^{-m_2}, \quad (11)$$

160 where  $m_2$  is a constant ranging between 1.8 and 2 for sandstones.

161 Fig. 5 shows the computed two-point correlation function for the CB sandstone images. For each  
 162 sample, four curves are displayed, corresponding to the whole 3D image and three 2D cross-sections

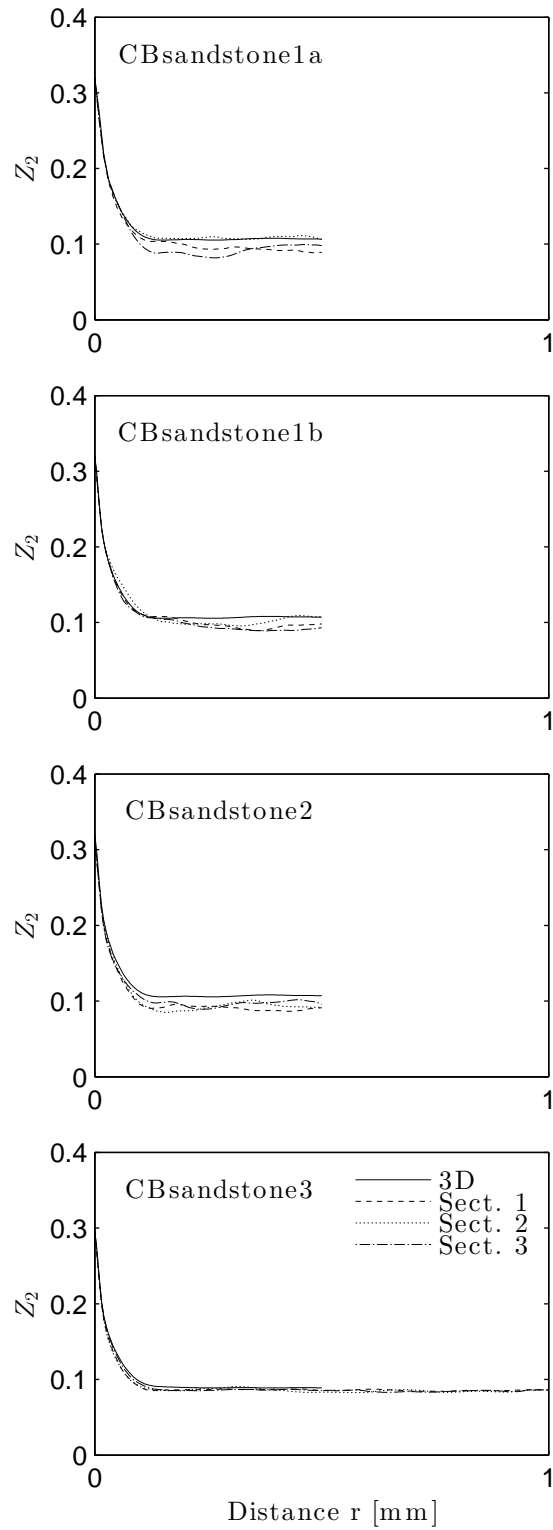


**Figure 5.** Computed two-point correlation function for the CB sandstone samples. For each sample, four curves are displayed, corresponding to the whole 3D image (continuous line) and three 2D cross-sections chosen with the same areal porosity as the volumetric one



165 chosen with the same areal porosity as the volumetric one. The 3D curve is computed using eqs. (5)  
 166 and (6), while the 2D curves are computed using (3) and (4). The 3D curve smoothly approaches the  
 167 asymptotic value of  $\phi^2$  with the same trend for all the samples, suggesting that for this rock 1 mm<sup>3</sup> can  
 168 be assumed as REV for the pore geometry. However, for the smaller samples (CBsandstone1a, 1b and 2,  
 169 having all volume of 1 mm<sup>3</sup>), the 2D curves behave differently from the 3D one. They all show a distinct  
 170 minimum corresponding to the mean grain size and then tend to their respective asymptotic value with  
 171 an oscillatory behaviour. This discrepancy vanishes for the bigger sample (CBsandstone3 having volume  
 172 of 8 mm<sup>3</sup>), suggesting that 4 mm<sup>2</sup> can be assumed as representative area (REA).

173 The same analysis has been conducted on the carbonate images. The computed two-point correlation  
 174 functions are shown in Fig. 6. As for the CB samples, the 2D curves show an oscillatory behaviour which  
 175 is progressively damped with increasing the size of the sample. However, existence of an REV and REA  
 176 for this rock remains undetermined, due to the significant variability of the carbonate pore system. This  
 177 heterogeneity is made clearer by plotting the predicted mean pore radius, computed using eq. (9), as  
 178 a function of the image characteristic size, for all the processed images (Fig. 7). For each sample, 10  
 179 values are reported: one for the whole 3D image, and three for each of the three orthogonal directions,  
 180 i.e. three 2D cross-sections for each direction. For the CB sandstone a homogenous value in the range of  
 181 35-45  $\mu\text{m}$  is obtained, corresponding to a mean pore diameter of 70-90  $\mu\text{m}$ , in agreement with the value  
 182 of 100  $\mu\text{m}$  based on SEM images observations given by Lamy-Chappuis et al. (2014). On the other hand,  
 183 a larger dispersion is observed for the carbonate. In particular, a drop on the predicted mean pore size  
 184 is observed for the biggest 3D image. This is due to the heterogenous nature of this rock reflected by the  
 185 presence of large lithological clusts (see Figure 1b) which were not picked up by the smaller size images.  
 186 The range of predicted pore radius <60-130>  $\mu\text{m}$  corresponds to mean pore diameters of <120-260>  
 187  $\mu\text{m}$  which falls into the broader interval of 90  $\mu\text{m}$  to 700  $\mu\text{m}$  observed in SEM images. Furthermore, the  
 188 mean grain size predicted by the two-point spatial correlation function, i.e. the minimum value of  $Z_2$   
 189 in its initial descending branch, ranging between 240 and 380  $\mu\text{m}$ , is also in good agreement with the  
 190 morphological data (200-480  $\mu\text{m}$ ), obtained using a standard petrographic microscope. This confirms the  
 191 effectiveness of the method in fully characterizing the pore-system.

192 In order to assess anisotropy, we sampled the two-point correlation function only following the orthog-  
 193 onal directions, as in Yeong and Torquato (1998) and Øren and Bakke (2002). We than averaged these  
 194 components to obtain a function for the whole medium, and compared this with the one-dimensional  
 195 isotropic function computed using the extended Berryman's method for 3D images, eq. (5). Results are  
 196 shown in Figs. 8 and 9 for the sandstone and carbonate samples respectively. One striking aspect is that  
 197 sample Carb500 is strongly anisotropic. Fig. 9 clearly shows how the 3 directional functions have all  
 198 different slope in their initial descending branch. This is the only sample displaying this feature. Another  
 199 aspect which is worth highlighting is that the average directional  $Z_2$  is very close to the Berryman's one-  
 200 dimensional isotropic function. The latter has obviously a smoother profile, as sampling is done along  
 201 multiple directions. However, sampling along multiple directions has a very high computational cost,  
 202 which makes Torquato's method preferable.

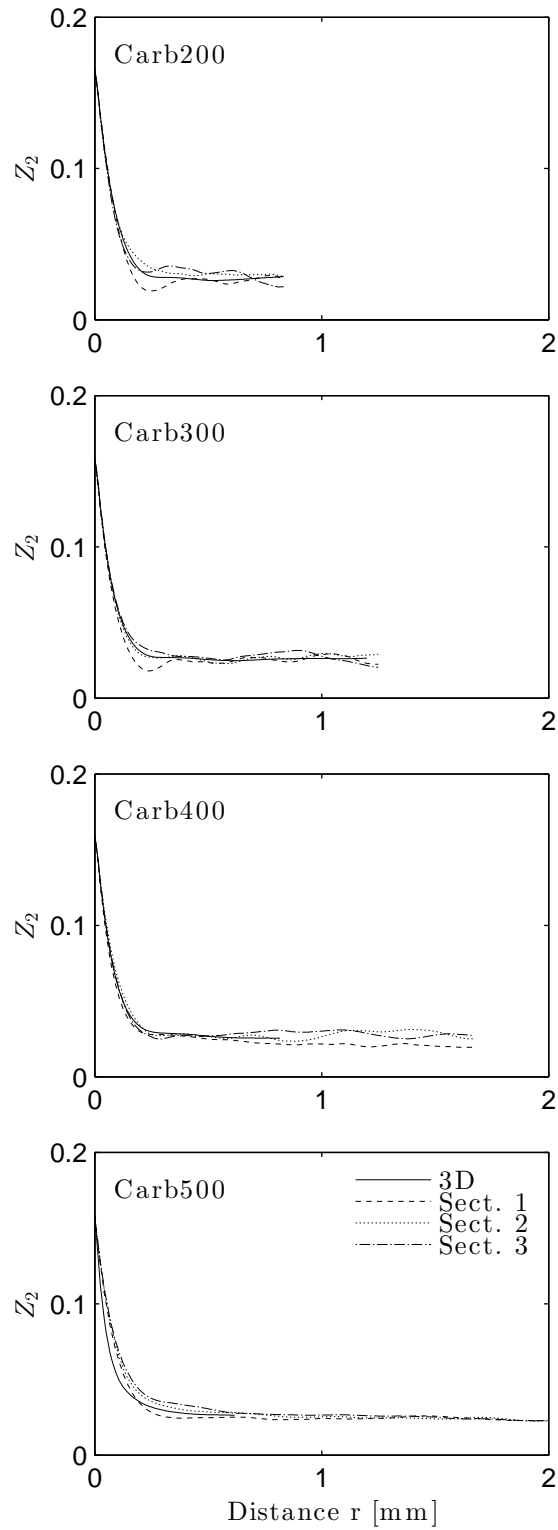


**Figure 6.** Computed two-point correlation function for the carbonate samples. For each sample, four curves are displayed, corresponding to the whole 3D image (continuous line) and three 2D cross-sections chosen with the same areal porosity as the volumetric one

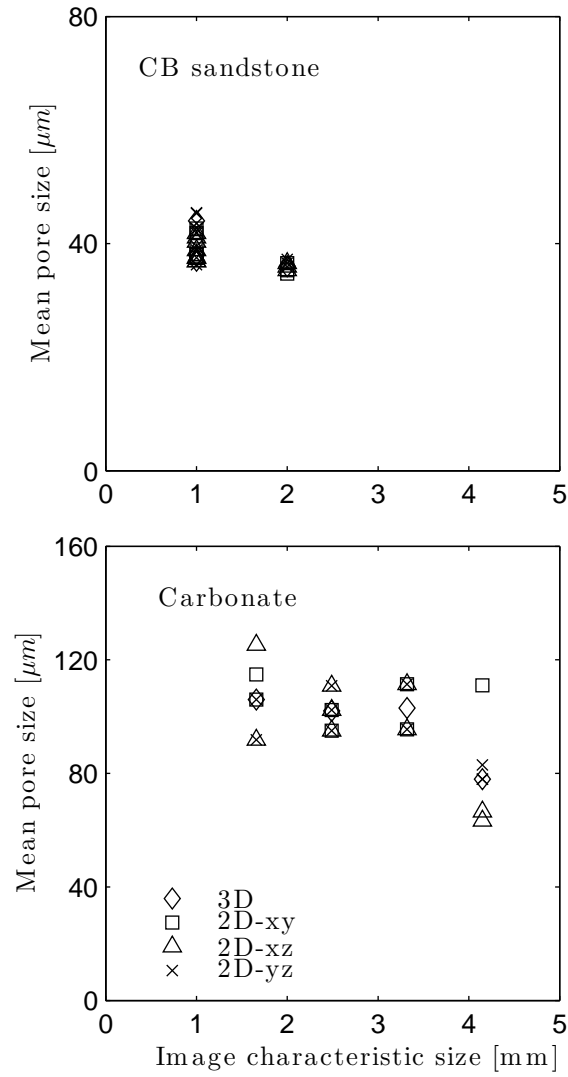


**Figure 7.** Summary of the estimated mean pore size for all the samples considered in this study. For each sample, 10 values are reported: one for the whole 3D image, and three for each of the three orthogonal planes, corresponding to the three selected 2D cross-sections for each plane

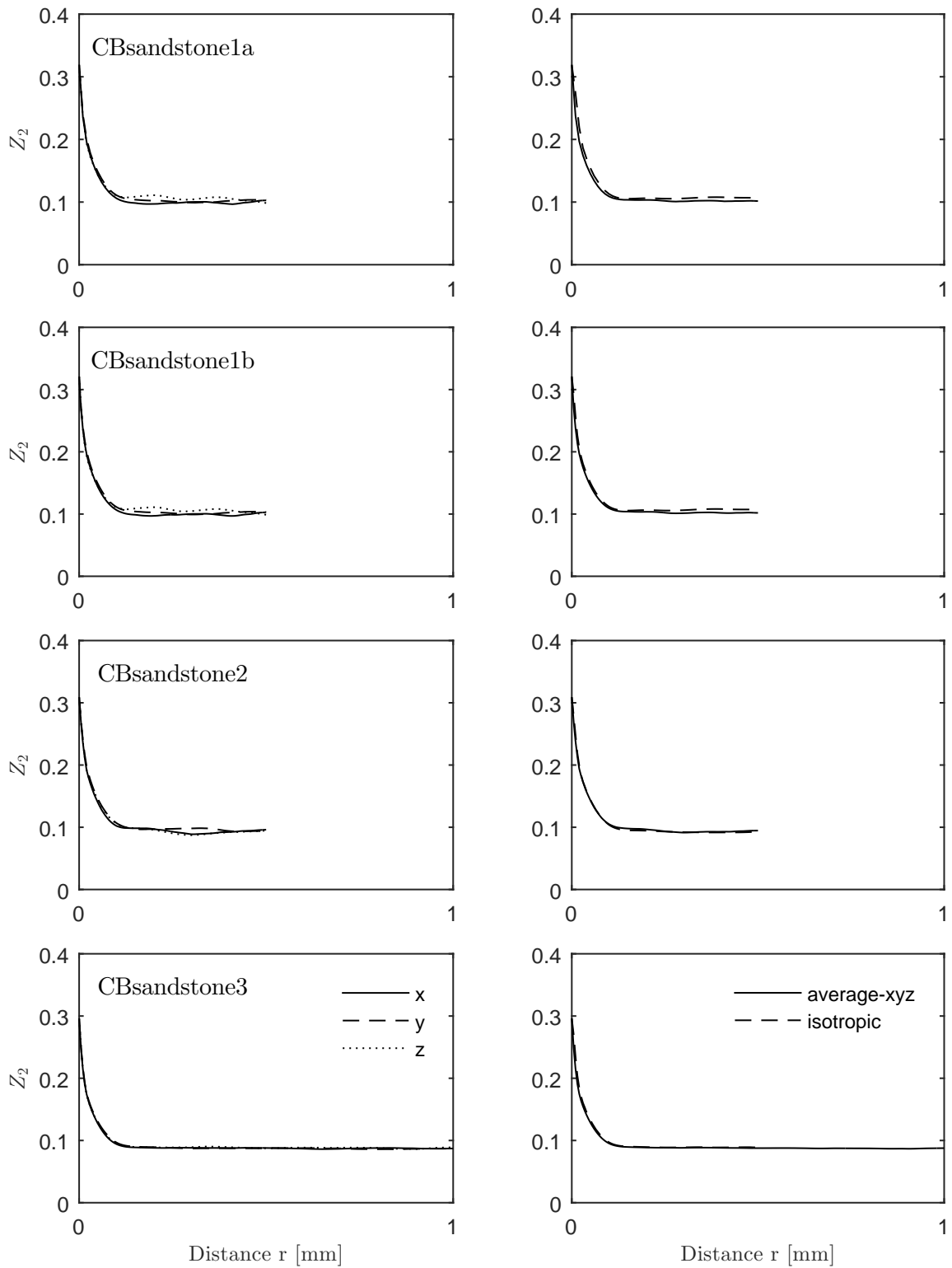


**Figure 8.** Directional two-point correlation functions (left column) and comparison between the average directional and the 3D isotropic Berrymans's function (right column) for the sandstone samples

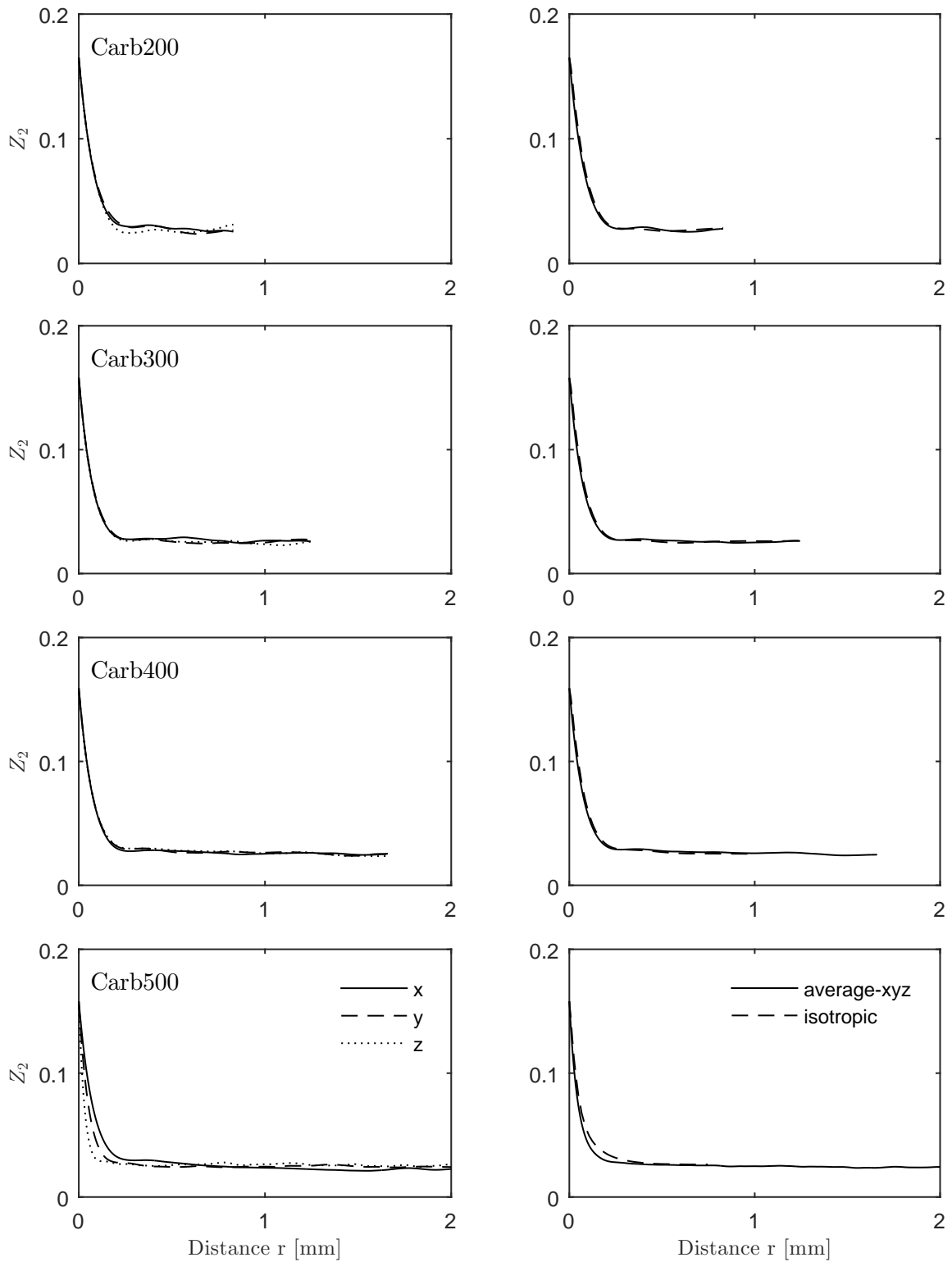


**Figure 9.** Directional two-point correlation functions (left column) and comparison between the average directional and the 3D isotropic Berrymans's function (right column) for the carbonate samples

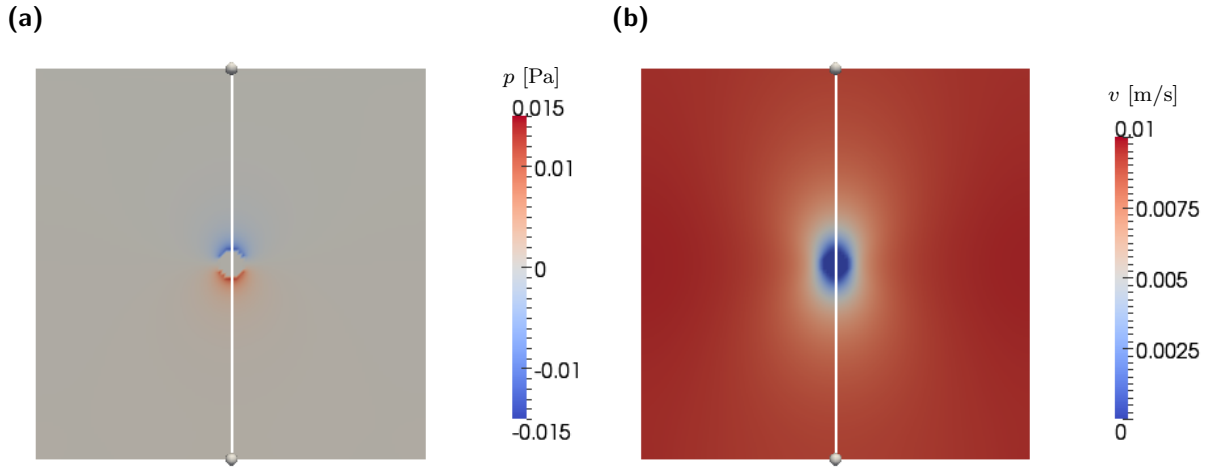


**Figure 10.** Predicted pressure (a) and velocity component in the direction of the flow (b) on a cross-section parallel to the main flow direction passing through the centre of the sphere. The flow is directed upwards along the depicted line

## 4. Computation of fluid flow and permeability prediction

### 4.1. Numerical method

The Stokes equations of creeping flow for incompressible fluids are written as

$$\nabla \cdot \mathbf{u} = 0, \quad (12)$$

$$\mu \nabla^2 \mathbf{u} - \nabla p + \rho \mathbf{g} = 0, \quad (13)$$

where  $\mathbf{u}$  is the velocity vector,  $p$  is the pressure,  $\rho$  and  $\mu$  are the fluid density and viscosity respectively, and  $\mathbf{g}$  is the acceleration of gravity vector.

We solve the incompressible Stokes equations using the FV-SIMPLE algorithm by Patankar (1980) on non-staggered grids.

### 4.2. Validation

The numerical model has been validated considering the Stokes flow past a sphere benchmark problem. For this test, a fluid of viscosity  $\mu = 0.001$  Pa·s flowing around a sphere of radius  $R=1$  mm with freestream uniform velocity  $v_0=0.01$  m/s was considered. The computational domain is a cube of size  $2L^3$  centered at the sphere centre, where  $L = 15R$  is the distance of the inlet boundary from the centre of the sphere, and was discretized using cubic cells of resolution  $R/\Delta x = 4$ , where  $\Delta x$  is the size of the elementary cell. Boundary conditions consist of the freestream uniform velocity at the inlet, prescribed pressure at the outlet and symmetry at the other 4 faces. The numerically evaluated pressure and velocity fields on a cross section passing through the centre of the sphere are shown in Figs. 10a and 10b respectively. Comparison between numerical and analytical values is made in terms of normalized pressure and velocity along the line depicted in Fig. 10. Velocity and pressure are normalized against the freestream uniform velocity  $v_0$  and the maximum value of pressure at the sphere  $p_{max} = 1.5\mu v_0/R$  respectively, while the x-axis, representing the distance  $r$  of a point from the centre of the sphere, is normalized against  $L$ . As Fig. 11 clearly shows, numerical results are in good agreement with the analytical solution, and only small errors can be ascribed to the influence of the boundary conditions and the poor discretization of the sphere.

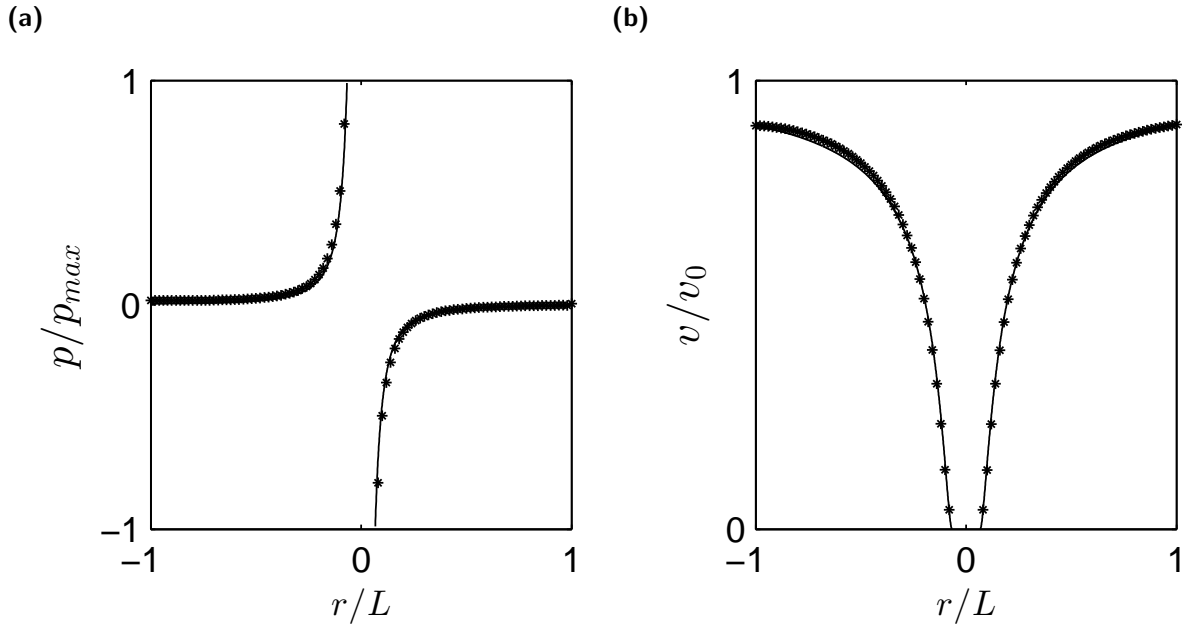


**Figure 11.** Comparison between analytical and predicted pressure (a) and velocity component in the direction of the flow (b) along the line depicted in Fig. 10. Legend: continuous line is the analytical solution, asterisk marks are the predicted values

### 227 4.3. Results

228 We present here results of the simulations carried out on the three dimensional images listed in Table  
 229 1. Boundary conditions consist of an applied pressure gradient along the main direction, symmetry at  
 230 the other four faces and no-slip conditions at the pore-grain interfaces. Internal connectivity of the  
 231 porous microstructure was assessed before starting the simulations, and isolated dead-end pores (pores  
 232 that are not connected to the boundary) were set as grains. Furthermore, in order to predict fluid flow  
 233 more accurately, the original digital images were refined by subdividing each voxel into up to 64 sub-  
 234 voxels. Predicted pressure field and velocity in form of streamlines are shown in Figs. 12 and 13 for the  
 235 CBSandstone1a and Carb300 samples respectively.

236 Permeability is then predicted from the computed fluid flow using Darcy's law as follows:

$$K = \mu \frac{QL}{A\Delta p}, \quad (14)$$

237 where  $Q$  is the flow rate,  $A$  is the area of the face normal to the flow,  $\mu$  is fluid viscosity and  $\Delta p/L$   
 238 is the applied pressure gradient. For a structured cubic grid of characteristic size  $L = N\Delta x$  and area  
 239  $A = N^2\Delta x^2$ , permeability is calculated as

$$K = \mu \frac{\Delta x}{N} \frac{\sum_j u_j}{\Delta p}, \quad (15)$$

240 where  $u_j$  is the velocity component in the direction of the flow and the sum is over all the pore cells on a  
 241 plane normal to the flow direction. Constant values of  $\mu=0.001$  Pa.s and  $\Delta p=1$  Pa were used in all the  
 242 simulations.

243 Anisotropy was also evaluated by running three separate simulations with applied pressure gradient  
 244 along each of the three orthogonal directions, and then calculating the following anisotropy ratio (Clavaud

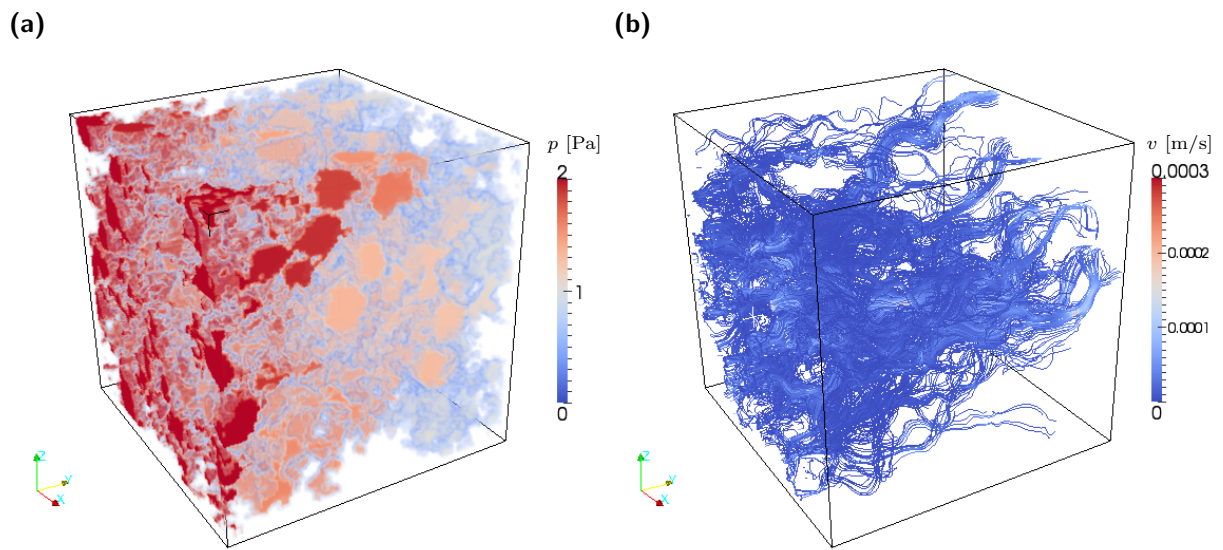


**Figure 12.** Predicted pressure field (a) and velocity in form of streamlines (b) for the sample CBsandstone1a

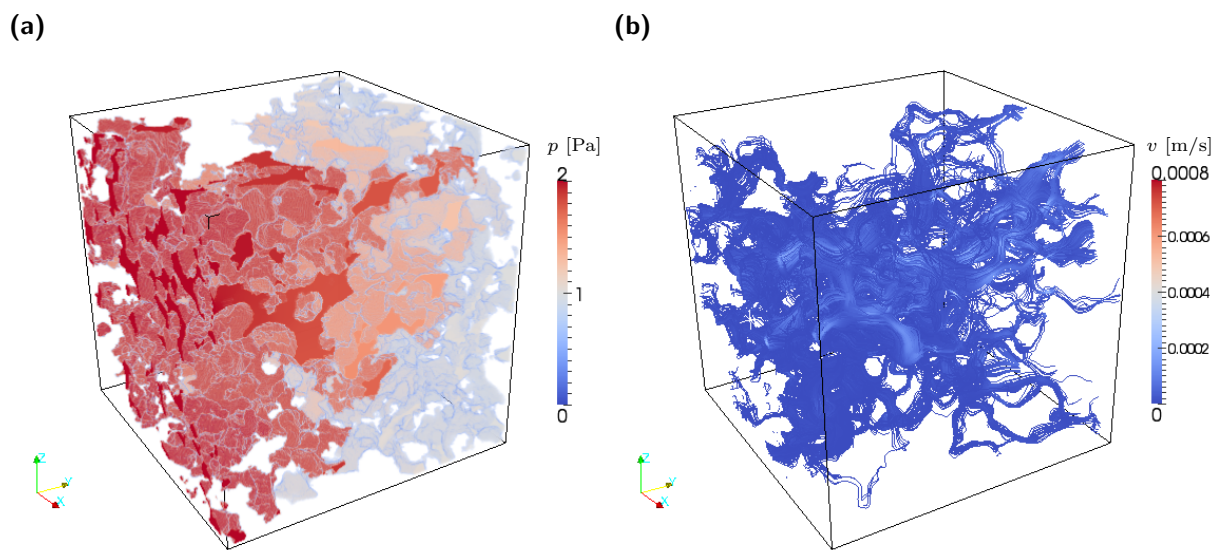


**Figure 13.** Predicted pressure field (a) and velocity in form of streamlines (b) for the sample Carb300



**Table 2.** Predicted permeability for all the samples considered

Sample	$K_x$ [Da]	$K_y$ [Da]	$K_z$ [Da]	$\nu$
CBsandstone1a	1.13	1.30	0.84	0.69
CBsandstone1b	1.13	1.36	0.84	0.68
CBsandstone2	0.87	1.06	0.85	0.88
CBsandstone3	0.86	1.05	0.91	0.88
Carb300	2.05	3.17	1.76	0.69
Carb400	2.99	2.70	2.76	0.94
Carb500	0.90	1.46	0.18	0.15

et al., 2008):

$$\nu = \frac{K_{min}}{\sqrt{K_{max}K_{int}}}, \quad (16)$$

where  $K_{max} > K_{int} > K_{min}$  are the three components of the permeability tensor along the three orthogonal directions  $x, y, z$ , sorted in descending order.

The predicted permeability values are listed in Table 2. For the CB sandstone, permeability remains constant in the narrow range  $< 0.8 - 1.2 >$  Da with increasing the size of the volume and for different locations of the samples, confirming the homogeneity of the rock and the REV of  $1 \text{ mm}^3$  observed using statistical correlation. Anisotropy also disappears for the biggest volume considered. As far as the carbonate is concerned, strong anisotropy is observed for the biggest sample (Carb500) and no clear determination of an REV for this rock can be made. Results in Table 2 confirm the findings reported in previous section, particularly as far as anisotropy of sample Carb500 is concerned.

#### 4.4. Comparison of different permeability estimates

We present here a comparison of all the available permeability estimates for the two rock formations considered. Fig. 14 shows the estimated values plotted against the experimentally determined value, the latter measured on the larger core plugs. The FV value has been computed as mean value of the 3 components listed in Table 2, while the KC value has been calculated using eq. (10). An estimated value from LBM simulations is also available for the CB sandstone only (pers. comm.).

For the carbonate sample, the measured permeability ( $\sim 1500$  mDa) is roughly twice as much the average FV value of  $\sim 850$  mDa computed for the largest sample Carb500, while is roughly half the average FV value of  $\sim 2800$  mDa computed for the smaller Carb400 sample. This inconsistency is probably due to the already highlighted heterogeneity of the rock, as well as the difference in scale of the samples, resulting in significant changes in connectivity and tortuosity.

For the CB sandstone, a good agreement between permeability estimates obtained from different numerical approaches (i.e. FV and LBM) is observed. However, divergence up to almost two orders of magnitude appears between the predicted values and the experimentally determined permeability of  $\sim 10$  mDa. Again, this discrepancy can be attributed to the complex microstructure of the rock and the presence of micro-imperfections, i.e. calcite shells fragments (Lamy-Chappuis, 2015), that cannot be detected by the resolution used for scanning the samples. As a result, very intricate pores filled with sub-micro fragments, which in reality have very high pore-grain surface area and very low net pore-volume, are converted into large open pores during the segmentation process, resulting in a much greater predicted permeability than the actual one. The thresholding used for segmentation of the X-

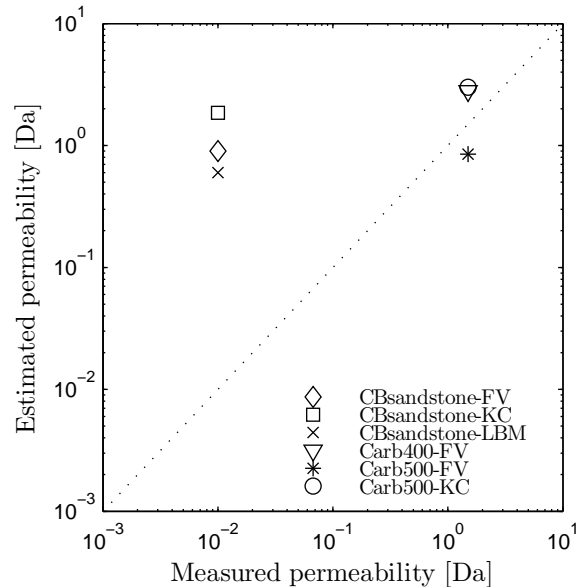


Figure 14. Comparison of different permeability estimates

275 rays  $\mu - CT$  images is another source of uncertainty and might influence the permeability. However,  
 276 despite ongoing developments and recent introduction of new algorithms, the segmentation of X-rays  
 277  $\mu - CT$  images of porous materials is still a controversial research field, and there is no evidence that  
 278 more advanced methods are better than global thresholding for fluid flow modelling (see Iassonov et al.  
 279 (2009); Wildenschild and Sheppard (2013) for more details on this subject).

280 Finally, the KC equation fitted with the specific surface area value estimated using statistical corre-  
 281 lation gives results close to the numerical ones for both rock formations. However, it must be noted that  
 282 eq. (10) relies on the constants  $m_1$  and  $m_2$ , whose calibration depends upon the morphological features  
 283 of the rock. For example, for the sample CBSandstone3, using the range of reference values for  $m_1$  and  
 284  $m_2$  given in literature (Archie et al., 1942; Walsh and Brace, 1984) produced permeability values ranging  
 285 from 1230 to 2360 mDa. The lower limit is very close to the average numerical permeability of 940 mDa.  
 286 A perfect fit could be obtained for values of  $m_1$  and  $m_2$  equal to 3.1 and 2.2 respectively, or, working on  
 287  $m_2$  only, to 3 and 2.22. This latter result also shows how eq. (10) is more sensitive to  $m_2$  than  $m_1$ . This  
 288 is because  $m_2$  is related to the formation factor, which is a key quantity describing the pore-structure of  
 289 a rock, while  $m_1$  depends on the shape and roughness of the pores, and can always be reasonably taken  
 290 as equal to its upper limit. For the carbonate, the analysis is similar. For the sample Carb400, using  
 291 the reference values of  $m_1$  and  $m_2$  yielded a range of permeability values from 3500 to 7590 mDa. Again  
 292 the lower limit is closest to the average numerical permeability of 2800 mDa, and the fit is obtained for  
 293 values of  $m_1$  and  $m_2$  equal to 3 and 2.12 respectively.

## 294 5. Bulk momentum balance and a new coverage criterion for the SIMPLE algorithm

295 The traditional convergence criterion for the SIMPLE algorithm utilizes the continuity imbalance,  
 296 i.e. the r.h.s. of the artificially built pressure-correction equation, as a residual. It is then demanded  
 297 that its normalization to an appropriate quantity be less than a given tolerance (Patankar, 1980; Perić  
 298 et al., 1988). For example, Mostaghimi et al. (2013) proposed as a convergence criterion to check the

299 normalized continuity imbalance (NCI), defined as the ratio of the average continuity imbalance  $\bar{b}_c$  over  
 300 the average flow rate  $\bar{Q}$  as follows:

$$NCI = \frac{\bar{b}_c}{\bar{Q}}, \quad (17)$$

301 and to terminate the computation when NCI is less than a given tolerance  $\lambda$ . Alternatively, a general  
 302 stopping criterion based on the reduction of the residual can be used (Ferziger and Peric, 2012). In this  
 303 case, iterations are stopped when the average residuals of all equations, namely pressure-correction and  
 304 x, y, z momentum, are reduced to a given fraction of its original size. However, both these criteria are  
 305 based on local satisfaction of the governing equations, and no information is provided at the macroscopic  
 306 level. The latter aspect is of particular interest for pore-scale modelling of reservoir rocks, especially when  
 307 one wants to use the pore-scale results for upscaling over REV's, as in case of permeability estimation.  
 308 Darcy's law, which is used here, is indeed none other than expression of the macroscopic momentum  
 309 balance (Whitaker, 1986).

310 Let us write the momentum equation (13) integrated over a control volume V having boundary area  
 311 A as follows:

$$\mu \int_A \frac{\partial u_j}{\partial x_i} n_i dA - \int_A p n_j dA + B = 0, \quad (18)$$

312 where n is the unit normal pointing outwards the surface and B accounts for body forces. Considering  
 313 the whole bulk medium as control volume, each of the two areal integrals in eq. (18) can be decomposed  
 314 into two sub-integrals: one over the external boundary pore area  $A_p$  and one over the internal pore-grain  
 315 interfacial area  $A_s$ . The momentum equations for the whole medium can therefore be written as

$$\mu \int_{A_p} \frac{\partial u_j}{\partial x_i} n_i dA - \int_{A_p} p n_j dA + \mu \int_{A_s} \frac{\partial u_j}{\partial x_i} n_i dA - \int_{A_s} p n_j dA + B = 0. \quad (19)$$

316 The first term in eq. (19) is zero because of the applied boundary conditions (zero velocity-gradient at  
 317 boundaries where pressure is prescribed and symmetry at the other four faces). The second term is the  
 318 macroscopic force due to the applied pressure difference  $\Delta P$ . The third and fourth terms are usually  
 319 referred to as the viscous (or friction) drag  $D_v$  and the pressure (or form) drag  $D_p$  respectively. Eq. (19)  
 320 in its compact form  $\Delta P + B = D_p + D_v$  represents a balance of forces at the macroscopic level and must  
 321 be satisfied by the solution of the Stokes equations (12)-(13).

322 Hence, the proposed convergence criterion consists on monitoring the Relative Error in the Bulk  
 323 Momentum Balance (REBMB) defined as

$$REBMB = \left| \frac{\Delta P + B - (D_p + D_v)}{\Delta P + B} \right|. \quad (20)$$

324 This new criterion has the major merit of giving a clear physical interpretation of the approximate  
 325 solution, i.e. how close one is to satisfy the bulk momentum balance and therefore how confident one can  
 326 be in using Darcy's law for predicting the absolute permeability. This makes the criterion particularly  
 327 useful for pore-scale modelling of reservoir rocks.

328 To test the new convergence criterion, we performed a test on the sample CBSandstone1b. Results  
 329 are shown in Fig. 15. We monitored four quantities: the normalized average residuals of the momentum

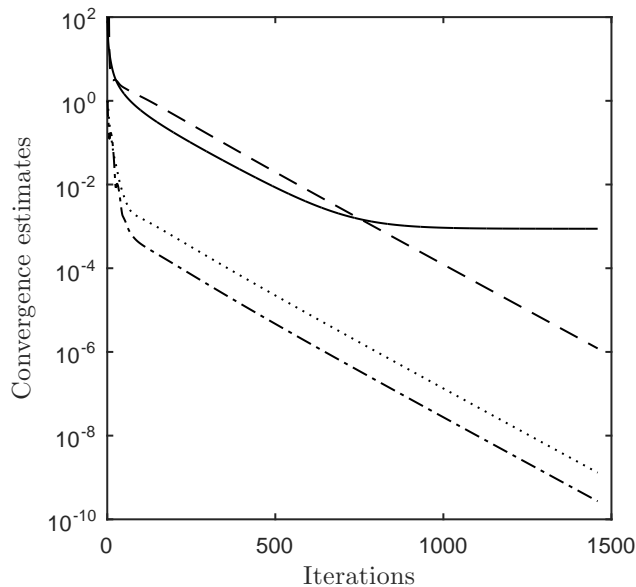


**Figure 15.** Comparison of different convergence indicators as a function of the outer iterations in the SIMPLE algorithm. Solid line: REBMB computed using eq. (20). Dashed line: NCI computed using eq. (17). Dotted line: normalized average residual of the momentum component in the direction of the flow. Dash-dot line: normalized average residual of the pressure-correction equation

330 component in the flow direction and pressure-correction equations, the normalized continuity imbalance,  
 331 eq. (17), and the proposed REBMB, eq. (20). As the graph clearly shows, the normalized average  
 332 residuals of both equations keep decreasing linearly as the solution of the respective PDE improves. NCI  
 333 displays a similar behaviour. The REBMB instead converges to an asymptotic value as the macroscopic  
 334 balance of forces in the flow direction can no longer be further refined with additional iterations. The  
 335 achieved REBMB is less than 0.07% which can be considered an accurate measure. The fact that an  
 336 asymptotic value is reached offers a valuable stopping criterion, provided that continuity must be satisfied  
 337 as well. In light of this, the best convergence criterion appears to be a combination of the new one based  
 338 on bulk momentum balance and the classical ones based on residual reduction. A suggested stopping  
 339 criterion would be the scenario where the asymptotic value of REBMB is reached and the residuals have  
 340 been reduced by 4-5 order of magnitude. Finally, it must be noted that this overall convergence criterion is  
 341 only related to the quality of the final approximate solution and does not impact the optimum computing  
 342 time, the latter being determined primarily by the method for the solution of the linear systems.

## 343 6. Conclusions

344 We presented here an integrated approach comprising computer tomography, statistical correlation  
 345 and numerical simulations, for predicting the petrophysical properties, namely REV, permeability and  
 346 mean pore size, of different reservoir rocks. We used the two-point spatial correlation function to analyze  
 347 the pore-system and the FV-SIMPLE algorithm to solve the Stokes equations of flow. By analyzing  
 348 several binarized small samples (order of mm) scanned at a resolution down to  $5 \mu\text{m}$ , we showed the  
 349 potential of this approach to provide thorough characterization of reservoir rocks. The two-point spatial  
 350 correlation function was shown to be an effective way for estimating REV and REA, as well as a powerful  
 351 method for evaluating the mean pore and grain sizes. Using these tools, pore sizes of  $70\text{-}90 \mu\text{m}$  for the

352 sandstone and 120-260  $\mu\text{m}$  for the carbonate were estimated, in good agreement with the respective values  
353 of 100  $\mu\text{m}$  and from 90  $\mu\text{m}$  to 700  $\mu\text{m}$  measured from high resolution SEM images. For the carbonate,  
354 comparison of grain size was also made, showing good agreement between the statistically estimated  
355 values of 240-380  $\mu\text{m}$  and the morphological data of 200-480  $\mu\text{m}$  obtained using a standard petrographic  
356 microscope. Rock homogeneity and anisotropy were also effectively evaluated using spatial correlation  
357 tools. This can be very helpful when selecting the most representative sample for use in more sophisticated  
358 numerical analyses. Moreover, this approach could be used to link the configuration of the pore system  
359 to the petrophysical properties of rocks, in a similar way to what Kozeny-Carman relationships do, e.g.  
360 the heterogeneity of the carbonate pore-system reflects on the variability in the predicted permeability  
361 for different sizes of the sub-samples. Comparison of all the available permeability estimates revealed  
362 good agreement between different numerical estimates, i.e. FV and LBM, but a discrepancy with the  
363 experimentally measured value. The latter is probably due to the difference in scale of the samples,  
364 resulting in significant changes in connectivity and tortuosity. For the sandstone, this discrepancy is  
365 larger due to the complexity of the pore system, i.e. the presence of sub-micro imperfections that cannot  
366 be detected by the resolution used to resolve the pore-space. More samples from different rock formations  
367 therefore need to be studied in order to establish a relationship between permeability estimates at different  
368 scales. This can be subject of a future more comprehensive study.

369 Finally, we presented a new convergence criterion for the SIMPLE algorithm, and more generally for  
370 the family of pressure-correction methods, based on the bulk momentum balance. This criterion provides  
371 information into significant fluid mechanics quantities such as form and friction drags, and is particularly  
372 useful for pore-scale modelling of reservoir rocks, especially when the predicted flow quantities are used  
373 for upscaling, e.g. Darcy's law. Moreover, the distribution of the error as a function of the iterations  
374 showed an asymptotic behaviour. This provides a valuable stopping criterion when the new convergence  
375 indicator is effectively used in combination with classical normalized residuals.

## 376 **Acknowledgements**

377 This work was jointly sponsored by EPSRC (EP/I010971/1) and NSFC China.

378 Adler, P., Jacquin, C., and Quiblier, J. (1990). Flow in simulated porous media. *International Journal*  
379 *of Multiphase Flow*, 16(4):691–712.

380 Al-Omari, A. and Masad, E. (2004). Three dimensional simulation of fluid flow in x-ray ct images of porous  
381 media. *International Journal for Numerical and Analytical Methods in Geomechanics*, 28(13):1327–  
382 1360.

383 Archie, G. E. et al. (1942). The electrical resistivity log as an aid in determining some reservoir charac-  
384 teristics. *Transactions of the AIME*, 146(01):54–62.

385 Bakke, S., Øren, P.-E., et al. (1997). 3-d pore-scale modelling of sandstones and flow simulations in the  
386 pore networks. *Spe Journal*, 2(02):136–149.

387 Bear, J. (1972). Dynamics of fluids in porous media.

388 Berryman, J. G. (1985). Measurement of spatial correlation functions using image processing techniques.  
389 *Journal of Applied Physics*, 57(7):2374–2384.

390 Berryman, J. G. and Blair, S. C. (1986). Use of digital image analysis to estimate fluid permeabil-  
391 ity of porous materials: Application of two-point correlation functions. *Journal of applied Physics*,  
392 60(6):1930–1938.

393 Blunt, M. J., Bijeljic, B., Dong, H., Gharbi, O., Iglauer, S., Mostaghimi, P., Paluszny, A., and Pentland,  
394 C. (2013). Pore-scale imaging and modelling. *Advances in Water Resources*, 51:197–216.

395 Blunt, M. J., Jackson, M. D., Piri, M., and Valvatne, P. H. (2002). Detailed physics, predictive capa-  
396 bilities and macroscopic consequences for pore-network models of multiphase flow. *Advances in Water*  
397 *Resources*, 25(8):1069–1089.

398 Chen, S. and Doolen, G. D. (1998). Lattice boltzmann method for fluid flows. *Annual review of fluid*  
399 *mechanics*, 30(1):329–364.

400 Clavaud, J.-B., Maineult, A., Zamora, M., Rasolofosaon, P., and Schlitter, C. (2008). Permeability  
401 anisotropy and its relations with porous medium structure. *Journal of Geophysical Research: Solid*  
402 *Earth*, 113(B1).

403 Coelho, D., Thovert, J.-F., and Adler, P. (1997). Geometrical and transport properties of random packings  
404 of spheres and aspherical particles. *Physical Review E*, 55(2):1959.

405 Dong, H. (2008). *Micro-CT imaging and pore network extraction*. PhD thesis, Department of Earth  
406 Science and Engineering, Imperial College London.

407 Ferziger, J. H. and Peric, M. (2012). *Computational methods for fluid dynamics*. Springer Science &  
408 Business Media.

409 Frisch, U., Hasslacher, B., and Pomeau, Y. (1986). Lattice-gas automata for the navier-stokes equation.  
410 *Physical review letters*, 56(14):1505.

411 Guibert, R., Nazarova, M., Horgue, P., Hamon, G., Creux, P., and Debenest, G. (2015). Computa-  
412 tional permeability determination from pore-scale imaging: Sample size, mesh and method sensitivities.  
413 *Transport in Porous Media*, 107(3):641–656.

414 Haines, T. J., Michie, E. A., Neilson, J. E., and Healy, D. (2016). Permeability evolution across carbonate  
415 hosted normal fault zones. *Marine and Petroleum Geology*, 72:62–82.

416 Haines, T. J., Neilson, J. E., Healy, D., Michie, E. A., and Aplin, A. C. (2015). The impact of carbonate  
417 texture on the quantification of total porosity by image analysis. *Computers & Geosciences*, 85:112–125.

418 Iassonov, P., Gebrenegus, T., and Tuller, M. (2009). Segmentation of x-ray computed tomography images  
419 of porous materials: A crucial step for characterization and quantitative analysis of pore structures.  
420 *Water Resources Research*, 45(9).

- 421 Lamy-Chappuis, B. (2015). *Mineral-Fluid interactions and their implications for the sequestration of*  
422 *CO<sub>2</sub> in saline aquifers*. PhD thesis, University of Leeds.
- 423 Lamy-Chappuis, B., Angus, D., Fisher, Q., Grattoni, C., and Yardley, B. W. (2014). Rapid porosity and  
424 permeability changes of calcareous sandstone due to CO<sub>2</sub>-enriched brine injection. *Geophysical Research*  
425 *Letters*, 41(2):399–406.
- 426 Litster, S., Epting, W., Wargo, E., Kalidindi, S., and Kumbur, E. (2013). Morphological analyses of  
427 polymer electrolyte fuel cell electrodes with nano-scale computed tomography imaging. *Fuel Cells*,  
428 13(5):935–945.
- 429 Martys, N. S., Torquato, S., and Bentz, D. (1994). Universal scaling of fluid permeability for sphere  
430 packings. *Physical Review E*, 50(1):403.
- 431 Mostaghimi, P., Blunt, M. J., and Bijeljic, B. (2013). Computations of absolute permeability on micro-ct  
432 images. *Mathematical Geosciences*, 45(1):103–125.
- 433 Øren, P.-E. and Bakke, S. (2002). Process based reconstruction of sandstones and prediction of transport  
434 properties. *Transport in Porous Media*, 46(2):311–343.
- 435 Oren, P.-E., Bakke, S., Arntzen, O. J., et al. (1998). Extending predictive capabilities to network models.  
436 *SPE journal*, 3(04):324–336.
- 437 Otsu, N. (1975). A threshold selection method from gray-level histograms. *Automatica*, 11(285-296):23–  
438 27.
- 439 Patankar, S. (1980). *Numerical heat transfer and fluid flow*. CRC Press.
- 440 Perić, M., Kessler, R., and Scheuerer, G. (1988). Comparison of finite-volume numerical methods with  
441 staggered and colocated grids. *Computers & Fluids*, 16(4):389–403.
- 442 Politis, M., Kikkinides, E., Kainourgiakis, M., and Stubos, A. (2008). A hybrid process-based and  
443 stochastic reconstruction method of porous media. *Microporous and Mesoporous Materials*, 110(1):92–  
444 99.
- 445 Sabharwal, M., Pant, L., Putz, A., Susac, D., Jankovic, J., and Secanell, M. (2016). Analysis of catalyst  
446 layer microstructures: From imaging to performance. *Fuel Cells*, 16(6):734–753.
- 447 Tashman, L., Masad, E., Crowe, C., and Muhunthan, B. (2003). Simulation of fluid flow in granular  
448 microstructure using a non-staggered grid scheme. *Computers & fluids*, 32(9):1299–1323.
- 449 Valvatne, P. H., Piri, M., Lopez, X., and Blunt, M. J. (2005). Predictive pore-scale modeling of single  
450 and multiphase flow. In *Upscaling Multiphase Flow in Porous Media*, pages 23–41. Springer.
- 451 Walsh, J. and Brace, W. (1984). The effect of pressure on porosity and the transport properties of rock.  
452 *Journal of Geophysical Research: Solid Earth (1978–2012)*, 89(B11):9425–9431.

- 453 Whitaker, S. (1986). Flow in porous media i: A theoretical derivation of darcy's law. *Transport in porous*  
454 *media*, 1(1):3–25.
- 455 Wildenschild, D. and Sheppard, A. P. (2013). X-ray imaging and analysis techniques for quantifying pore-  
456 scale structure and processes in subsurface porous medium systems. *Advances in Water Resources*,  
457 51:217–246.
- 458 Yeong, C. and Torquato, S. (1998). Reconstructing random media. *Physical Review E*, 57(1):495.
- 459 Zaretskiy, Y., Geiger, S., Sorbie, K., and Förster, M. (2010). Efficient flow and transport simulations in  
460 reconstructed 3d pore geometries. *Advances in Water Resources*, 33(12):1508–1516.
- 461 Zu, Y. and He, S. (2013). Phase-field-based lattice boltzmann model for incompressible binary fluid  
462 systems with density and viscosity contrasts. *Physical Review E*, 87(4):043301.